AIAA SciTech Forum
January 3-7, 2022, San Diego, CA & Virtual
AIAA SCITECH 2022 Forum

10.2514/6.2022-1548

Swirl Characterization of a Cyclotronic Arc Plasma Actuated Axial Air Jet

Georgi K. Hristov*, Phillip J. Ansell†
University of Illinois at Urbana-Champaign, Urbana, Illinois 61801

and

Joseph W. Zimmerman‡, and David L. Carroll§
CU Aerospace, Champaign, Illinois 61820

A plasma swirler, based on an existing Lorentz force driven gliding arcs, was developed as a flame holding and combustion enhancing device for premixed and diffusion flames. The device is intended to deliver the combined benefits of jet swirlers and plasma assisted combustion by providing fluidic mixing to augment flame stability, and high energy particles to enhance the combustion process. The current study focused on characterizing the fluid dynamic effects of the plasma swirler on an axial air jet ejected at various air flow rates in quiescent air. Schlieren imaging was used to study the thermal effects of the plasma on the axial air jet and qualitatively compare the turbulence levels in the actuated and unactuated jets. Time-averaged stereoscopic particle image velocimetry data were acquired across seven evenly-spaced planes perpendicular to the exit plane of the plasma swirler at three different axial flow rates, while maintaining constant plasma swirling parameters. These data were used to reconstruct three-component volumetric averaged velocity fields. Two-dimensional cross sections along with three-dimensional isosurfaces of the mean flow were used to describe the induced flow and flow turbulence levels, and characterize the vorticity created by the swirler.

Nomenclature

B	=	magnetic flux density
D	=	orifice diameter
Q	=	volumetric flow rate
Q	=	Q-value
R	=	orifice radius
Re	=	Reynolds number
R_{ij}	=	Reynolds stress components; i and j correspond to the r, θ, and z coordinates
S_1, S_2, S_3	=	swirl number definitions
S_{ij}	=	strain rate tensor
u_i	=	velocity vector
V	=	voltage
V	=	velocity magnitude
V_z, V_θ, V_r	=	axial, tangential, and radial velocities
z, θ, r	=	axial, azimuthal, and radial coordinates
ν	=	kinematic viscosity
ρ	=	charge density
Ω	=	angular velocity

* Graduate Research Assistant, Department of Aerospace Engineering, Student Member, AIAA.
† Associate Professor, Department of Aerospace Engineering, Senior Member AIAA.
‡ Director of Plasmadynamics at CU Aerospace, Member AIAA.
§ President of CU Aerospace, Fellow AIAA.

Ω_{ij} = rigid body rotation rate tensor
ω = vorticity magnitude

I. Introduction

Swirling jets have been the subject of extensive research because they find use in many practical applications in devices with heat release such as furnaces and engines, plasma systems, chemical reactors, separators, etc. [1] Swirling jets are of particular interest especially in combustion, where swirling is needed to enhance mixing of the fuel and oxidizer, improve the heat and mass transfer, and augment flame stability. [2] A deeper understanding of the underlying physics associated with swirling flows has been important to inform design decisions when developing more efficient combustors and furnaces. Swirling flows with combustion have been shown to enhance performance by reducing undesirable effects such as noise and thermoacoustic resonance [3,4], by reducing hydrocarbon, CO, and NO_x emissions [5–7], and by extending the lean flame blow-off limits. [8]

Swirl increases the rate of spatial growth, the rate of entrainment, and the rate of decay of the jet. Swirling jets have also been associated with phenomena such as vortex breakdown and vortex core precession, which occur when the ratio of the azimuthal to axial momentum component exceeds a certain threshold. These flows have been extensively studied due to their potential beneficial effects on flames and combustors. [5] Therefore many studies have concentrated on high swirling jets and the associated vortex breakdown mechanisms. [9,10] Vortex breakdown is characterized by a destabilization of the vortex core, deceleration of the flow near the jet axis and the generation of an internal recirculation zone. [11] The low-velocity, low-pressure region in the core of the swirling flow provides favorable conditions for ignition and stable combustion. This highly turbulent region of recirculating flow can be used as a fluid-dynamical flame holder since it allows high rates of heat release as the incoming fuel and oxidizer are ignited by the recirculating hot combustion products. [12] Furthermore, the combustion lengths are reduced by the high rates of entrainment of the ambient fluid and fast mixing, particularly near to the boundaries of the recirculation zones. [1] The central vortex core in the recirculation zone can become unstable, giving rise to a precessing vortex core (PVC). [13] The precessing vortex core is another natural mechanism that can be used in lean premixed combustion to excite or increase periodic heat release. [13] It increases the turbulence and shear at the edge of the recirculation zone and consequently augments the mixing of air and fuel, which leads to efficient burning of poor quality and low-calorific fuels. [13,14] The improved mixing effects due to the PVC can be beneficial to combustion by improving the heat release efficiency and decreasing NO_x emissions. [15] Therefore, many researchers have looked into combustion and PVC effects. [16,17]

Although a lot of the research effort on swirling jets has concentrated on high swirl rates, swirl introduces a unique change in the boundary conditions of nearly all flow problems and even moderate amounts of swirl show enhanced mixing. Farokhi et al. [18] and Gilchrist and Naughton [19] showed that an axisymmetric jet with moderate swirl, below vortex breakdown, experienced enhanced growth rates and mixing in the near field, compared to a non-swirling jet. Enhanced growth rates for jets with low to moderate swirl can persist to 20 diameters downstream of the jet exit, even though the swirl has decayed to a point at which it is barely detectable [19].

Another way to stabilize the combustion process, increase the flame velocity, enhance the combustion efficiency, extend the blow-off limit of lean premixed flames, and reduce emissions is through plasma assisted combustion. [20,21] Plasma has been shown to be effective with a wide range of fuels such as methane, propane, and hydrogen. Its presence can drastically change the shape of the flame due to the plasma-induced body force, which along with the production of radicals, provides an effective means of decreasing the ignition time and increasing the flame stabilization. Therefore, many plasma-assisted configurations have been developed, ranging from dielectric barrier discharges [20,22] and nanosecond discharges [23–25] to plasma torches [26,27].

Magnetohydrodynamics (MHD), and more specifically the use of magnetic fields to apply forces on charged plasma particles, has been used in aerospace research with applications in fluid dynamic control [28–30] and plasma-assisted combustion. [31] A class of plasma devices called gliding arcs [32] and rail plasma actuators [33,34] apply the principles of MHD to arc plasma discharges. These actuators consist of parallel or diverging high-voltage rail electrodes which are mounted flush to an aerodynamic surface. The arc discharge that forms between the electrodes is linearly driven along the electrode gap by a magnetic field, induced either by the current through the rail electrodes or an external magnetic field from a permanent magnet. This type of device has been reported to induce flow velocities on the order of 10 m/s, which is larger than the induced flow velocities by DBD actuators. [35] Choi et al. [33]

successfully used streamwise rail plasma actuators for airfoil stall alleviation at Re = 45,000 and Re = 90,000. The authors reported 40% improvement in post-stall lift and 4° increase in stall angle compared to an unactuated case.

Based on the underlying principles of MHD, a novel cyclotronic arc-plasma actuator (CAPA) was jointly developed by CU Aerospace (CUA) and the University of Illinois at Urbana-Champaign (UIUC) for aerodynamic flow control. [36] This actuator employed a high-voltage breakdown between two coaxial electrodes positioned within the field of a strong rare-earth magnet. The breakdown filament was oriented relative to the magnetic field such that the Lorentz force on the charged plasma particles produced rotation about the center of the coaxial electrode assembly. Unlike other plasma actuators and gliding arc concepts which rely on adding momentum to the flow along a linear path set by the actuator orientation, the CAPA provided actuation through vorticity generation. Thus, aside from applications in aerodynamic flow control, the cyclotronic plasma actuator can be utilized in other areas where fluidic mixing and/or high-energy particles are necessary, such as plasma assisted combustion.

Kalra et al. [37] determined that an ideal plasma assisted combustion discharge is the gliding arc, as these devices typically generate plasma emissions with temperatures between thermal and nonthermal plasma. These intermediate temperatures are high enough for the ignition of a mixture, have activation benefits of a homogeneous discharge, provide high levels of chemical reaction selectivity, have high electron temperatures, and have high plasma densities with low power requirements. Therefore, a magnetically-stabilized, nonequilibrium gliding arc plasma discharge was used to treat air in counterflow methane-air diffusion flames. [38–40] Independently, Zimmerman and Carroll [41] modified a CAPA to create a similar coaxial gliding arc device to serve as a premixed flame holding device by integrating an injection in the coax through which the fuel and air are introduced and mixed by the discharge filament. The intent was to provide plasma swirling along with plasma assisted combustion, therefore, combining the beneficial effects of swirled flames and plasma enhanced flames. Following on from the existing research, the current investigation aims to fully describe and characterize the ability of the CAPA-type device to produce swirl in an axisymmetric jet of air. Therefore, the current fluid dynamic study will contribute to the better understanding of the mixing mechanisms manifested by the CAPA and similar flame holding devices.

II. Experimental Setup

A. Actuator Design

The plasma swirler used in the current study was an iteration of the cyclotronic arc-plasma actuator developed and described by Hristov et al. [36] that allowed for gas flow in the inter-electrode spacing. The design of the swirler, seen in Fig. 1, featured a coaxial configuration with a high voltage central electrode contained within a dielectric tube, and a grounded outer electrode placed within the inner diameter of a ring magnet. This configuration resulted in the production of a Lorentz force, which was applied to rotate the plasma discharge and actuate the flow. The magnet was sheathed from the electrodes by a dielectric surface. The assembly featured a 1.5-in outer diameter, 0.75-in inner diameter and was 0.75-in thick. The magnetic field at the top surface of the magnet was B = 4,900G.

The central high-voltage electrode was placed in the middle of the magnet thickness and a breakdown is therefore formed in the annular air gap between the electrodes, where the magnetic field was strongest and most uniform. In combustion applications, the fuel-air mixture would be injected through this annular gap and interact with the discharge. For the current fluid dynamic study, the gas that was used was air.

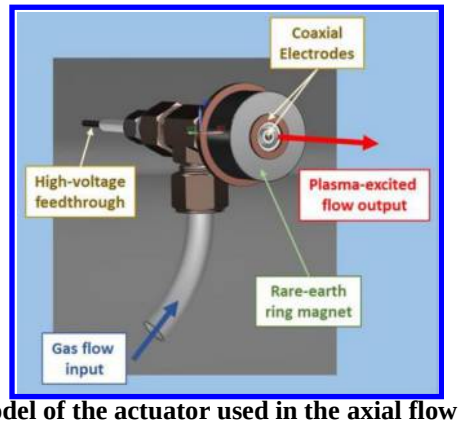

Fig. 1: A CAD model of the actuator used in the axial flow experiment. [41]

B. Actuator Circuit Characterization

A discharge was created in quiescent air using a zero-voltage-switching (ZVS) circuit powered by a DC supply, and a CRT transformer to produce high voltage. [42] Terminal measurements of the current-voltage (I-V) characteristics were acquired on the secondary transformer winding using a Pearson current monitor model 4100 and a Tektronix P6015 high voltage probe. The high voltage and secondary current data were probed at the lead that connected to the center electrode of the actuator. Measurements were made at four different input DC power levels with no air flow through the swirler, and additional measurements were acquired at four different flow rates of air for DC power supply levels of 73W.

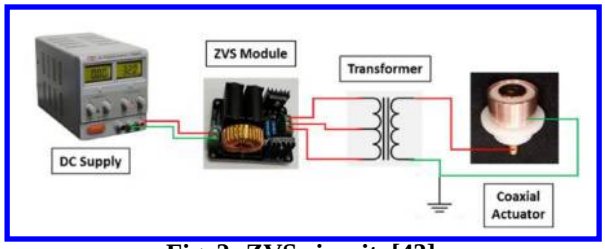

Fig. 2: ZVS circuit. [43]

C. Schlieren Visualization

Schlieren data were acquired for axial air flow interactions produced across the orifice of the CAPA swirler. A standard two-mirror schlieren setup, seen in Fig. 3 was used. This configuration included two parabolic mirrors, a point source of light, a vertical knife edge, and a high-speed camera. A Photron Mini AX200 high-speed camera equipped with a photographic lens was used to acquire schlieren images of the air jet at a frame rate of 6,400fps. The camera had an image size of 1,024 × 1,024 pixels and was operated at a shutter speed of 1/6,400s.

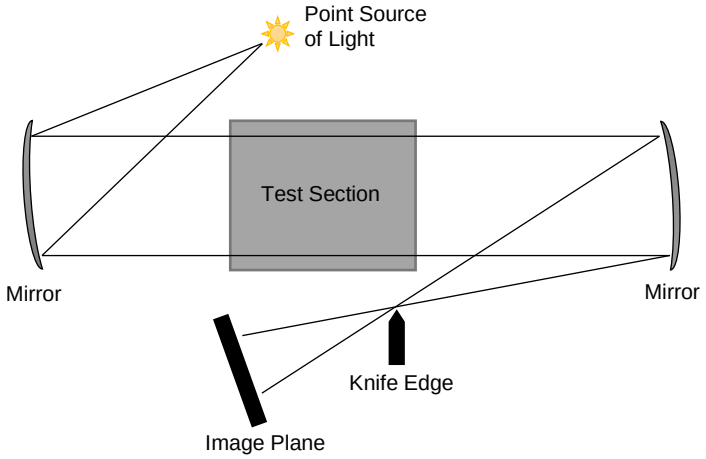

Fig. 3: A schematic of the schlieren setup.

D. Stereoscopic Particle Image Velocimetry

Time-averaged stereoscopic particle image velocimetry (Stereo-PIV) data of axial jet flow through the CAPA swirler were acquired in quiescent air. The swirler geometry was configured such that the magnet was flush with the swirler outlet, and the central high-voltage electrode was positioned at the center of the magnet thickness, which was 0.375in upstream from the outlet. Pictures of the setup and the swirler mounting are shown in Fig. 4a.

A motorized precision linear stage was used to traverse the image plane horizontally across the actuator in order to acquire velocity field data across a total of seven evenly-spaced PIV data planes (shown in Fig. 5b) such that the central plane was located at the center of the actuator and the two outer planes were tangential to the outermost edge of the outer electrode. This configuration resulted in just over 2mm spacing between PIV planes. A total of 2,100 three-component velocity vector fields were acquired across each PIV plane.

a) 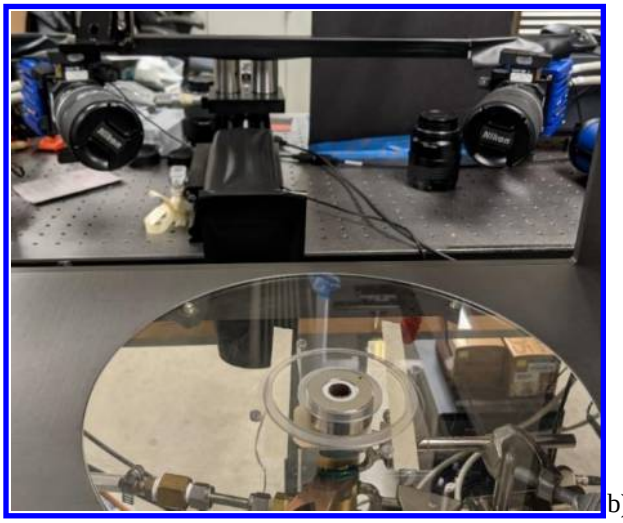 b) 

Fig. 4: a) PIV setup pictures: a) Swirler and cameras; b) Swirler mounting.

For time-averaged Stereo-PIV acquisition, the dual pulse repetition rate of the laser was set to 10 Hz. A New Wave Research Solo Nd:YAG laser was operated in external double trigger mode to provide a pair of laser pulses, separated by Δt = 150μs, 80μs, 60μs, or 40μs, depending on the air jet velocity. A series of beamforming optics were used to produce a laser sheet that illuminated the interrogation region. A ViCount oil-based smoke generator was used to seed the ambient air, and a TSI Six-Jet Atomizer 9306 was used to seed the axial air flow through the CAPA swirler. While there is a possibility that the plasma discharge resulted in an ionization of the seed particles, no particle charging effects were observed in the PIV measurements, and therefore this effect was assumed to be negligible. Two LaVision Imager sCMOS cameras with 2,560 × 2,160 pixel resolution were used to acquire images of the tracer particles. The angle between the cameras was set to be approximately 66°, according to the guidelines provided by Raffel et al., [44] in order to ensure high accuracy in the out-of-plane velocity component. Scheimpflug adapters were used to satisfy the Scheimpflug criterion. [45,46] Both cameras were equipped with identical photographic lenses with focal lengths of f = 135mm. The pulsed emissions of the laser and the frame acquisition of the cameras were triggered by a LaVision PTU-X timing unit. LaVision DaVis version 8.3 was used to calculate the vector fields. A multipass method was used, with an initial 96 × 96 pixel interrogation window with 50% overlap, which was decreased to a 16 × 16 interrogation window at 75% overlap in the final processing steps. Three-dimensional volumetric flowfields were produced by using Gaussian process regression between the planes where Stereo-PIV data were acquired.

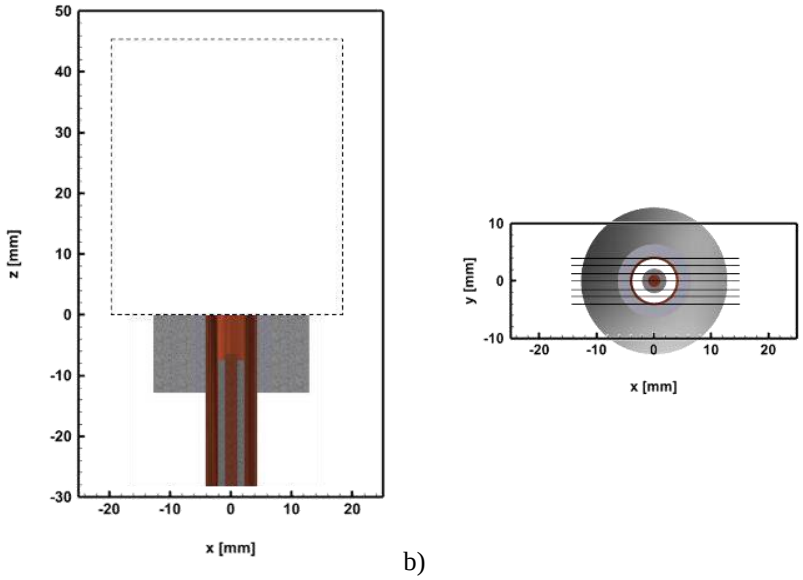

a) b)

Fig. 5: a) Interrogation region for PIV measurements; b) Locations of the PIV planes.

III. Results and Discussion

A. Jet Characterization Parameters

Two of the non-dimensional parameters that have historically been used to characterize swirling jets are the Reynolds number (Re) and the swirl number (S). [47] The Reynolds number is defined using the mean axial velocity of the jet at the exit (V_z), and the diameter of the orifice (D).

$$Re = \frac{V_z D}{\nu} \tag{1}$$

Various swirl number definitions exist, with each version being slightly different based on factors assumed to be important between different studies. Earlier studies established the swirl number to be the ratio of axial flux of angular momentum G_θ and axial flux of axial momentum G_z multiplied by the orifice radius R. This definition is often written in terms of the velocity components and the corresponding Reynolds stresses, which have often been neglected in earlier studies due to inability to accurately obtain these quantities:

$$S_1 = \frac{\int_0^R r^2(V_z V_\theta + R_{z\theta})dr}{R\int_0^R r(V_z^2 - 0.5V_\theta^2 + R_{zz} - 0.5(R_{\theta\theta} + R_{rr}))dr} \tag{2}$$

The aforementioned swirl number definition does not take into account the initial velocity profile of the jet, which has been demonstrated to be an important parameter dictating the characteristics of the jet. [18,48] Therefore, some researchers have considered this definition inadequate and have used other definitions that suit their particular studies. [47] For instance, Billant et al. [49] and Gallaire and Chomaz [50] used the ratio of the azimuthal velocity at the R/2 radial location to the centerline axial velocity at the jet exit:

$$S_2 = \frac{2V_\theta(\frac{R}{2}, x_0)}{V_z(0, x_0)} \tag{3}$$

Liang and Maxworthy [51] used the Taylor or inverse Rossby number, defined as the ratio between the azimuthal velocity to the axial velocity at the jet exit, to characterize the degree of swirl.

$$S_3 = \frac{\Omega R}{V_z} = \frac{V_\theta}{V_z} \tag{4}$$

Due to the coaxial geometry of the plasma swirler used in the current study, the jet axial velocity profile took the form of a double-hump profile, instead of the top hat profile used in the majority of swirling jet studies. The importance of the initial velocity distribution, discussed earlier, may make certain swirl number definitions unsuitable for the current study, e.g., S_2, because it considers the jet axial velocity at the center line, which is significantly lower for a double-hump profile than for a top hat profile with the same mean axial velocity. Therefore, due to the absence of a universal swirl number definition, and the various assumptions and limitations of the different definitions, the swirl number values presented in Table 1 will be only used for reference purposes and comparison to previous studies.

Table 1: Unactuated Jet Parameters.

Re	Q [LPM]	S_1	S_2	S_3
745	6	0.066	0.445	0.057
1,241	10	0.034	0.370	0.025
1,862	15	0.017	0.268	0.017
2,482	20	0.032	0.278	0.051

The setup was operated across a constant volumetric flow rate, and this condition was confirmed when turning the actuation on and off. The average exit flow velocity was calculated from the PIV data (Section III.D) for both the actuated and unactuated cases. The calculated exit velocity was consistently 15-20% higher for the actuated case, and this difference could not be explained solely by the uncertainty in the flow rate measurement, which was approximately 4%. The difference in the jet exit velocities is explained by the plasma blockage. Since plasma discharges influence the characteristics the surrounding air, notably in the form of a drag force component, researchers have previously suggested modeling the discharge as a solid or semi-porous body to a first order approximation. [40] Using this assumption along with geometric data of the arc from high-speed imaging (Section III.B), the blockage due to a body with the frontal section of the plasma filament was calculated. Using the jet exit area, known from geometry, and the plasma blockage area, the predicted jet exit velocities were calculated for both the actuated and unactuated cases. The results were within 4% of the actual velocity data, showing that the difference in initial velocity between the actuated and unactuated cases could be largely explained by the plasma blockage.

Table 2: Velocity due to Plasma Blockage.

Q [LPM]	$V_{experiment,\ no\ actuation}$ [m/s]	$V_{predicted,\ no\ actuation}$ [m/s]	Percent Error	$V_{experiment,\ actuation}$ [m/**s**]	$V_{predicted,\ actuation}$ [m/s]	Percent Error
10	1.80	1.87	-3.88%	2.21	2.24	-1.36%
15	2.52	2.55	-1.19%	3.06	3.06	0%
20	3.79	3.74	1.32%	4.47	4.31	3.58%

B. Discharge Visualization

An image of the plasma discharge as seen by eye under normal operation without axial flow is presented in Fig. 6a. The discharge appears as a uniform plasma disk to the common observer. High-speed imaging results of the no flow case, presented in Fig. 6b, show that the plasma disk is formed by a rotating plasma filament. The orientation of the magnetic field for the actuator used in the high-speed visualization was configured such that the plasma filament rotated in the clockwise direction. The curved shape of the discharge is consistent with the findings by Adams [52] for an electric arc rotating in a gas due to an external uniform magnetic field, and initially approximates an involute of a circle. The deviations from this predicted shape are attributed to electrode effects and the small inter-electrode gap. The high-speed image of the 10 LPM axial air flow case in Fig. 6c revealed an elongated filament with a larger curvature due to three-dimensional stretching of the discharge.

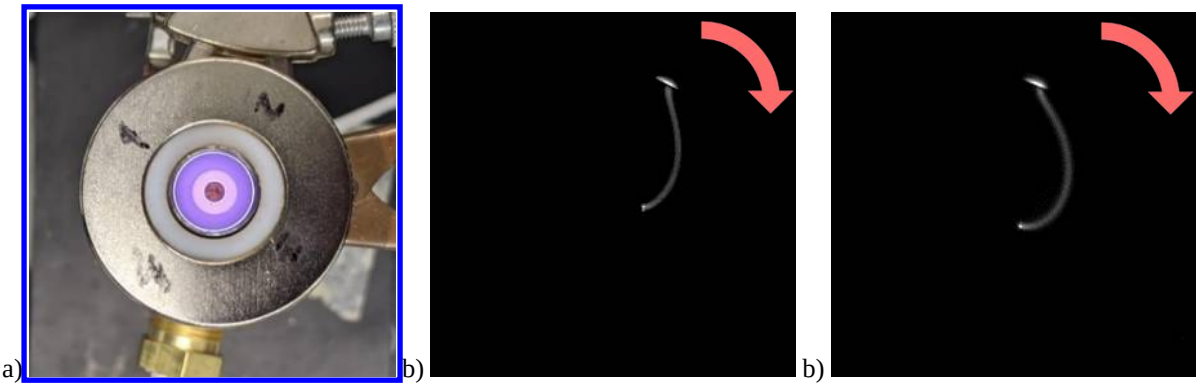

Fig. 6: Images of the plasma discharge: a) as seen by eye and no flow case; b) no flow case and exposure 20µs; c) 10 LPM of air flow case and exposure 20µs.

Tests of the discharge in quiescent air were conducted using the ZVS circuits driven by a DC power supply at different input power levels. The Lorentz forcing and therefore the discharge rotation rate was proportional to the power input. The results from the experiment are summarized in Table 3. High-speed visualization was performed on the discharge with air flow of 0 LPM, 6 LPM, 10 LPM, and 15 LPM. The images were used to calculate the corresponding rotation rates and the results were plotted in Fig. 7 as a function of the input DC power. The input DC voltage was kept constant across the different flow rates while the current depended on the power draw requirements of the discharge. Thus, as seen in the plot, higher flow rates resulted in higher current and therefore, higher power draw. A linear relationship existed between input DC power and rotation rate for the power levels tested. The rotation rate was highest for the no flow case and noticeably decreased for the flow-on cases. Little variation between the rotation rates for the different flow-on conditions at the same power level was observed. The decreased angular rate of the discharge rotation when in the presence of axial flow is attributed to the stretching and deflecting of the filament with respect to the magnetic field. The inner end of the filament was anchored to the end of the high voltage electrode and could not move in the axial direction; however, the outer grounded end of the filament could move in the axial direction as the ground electrode geometry allowed for it. Thus, in the presence of cross flow, the ground end of the discharge was deflected axially, in the same direction as the jet flow. This new orientation of the discharge was no longer perpendicular to the magnetic field lines and the Lorentz force, and therefore the rotation rate was decreased.

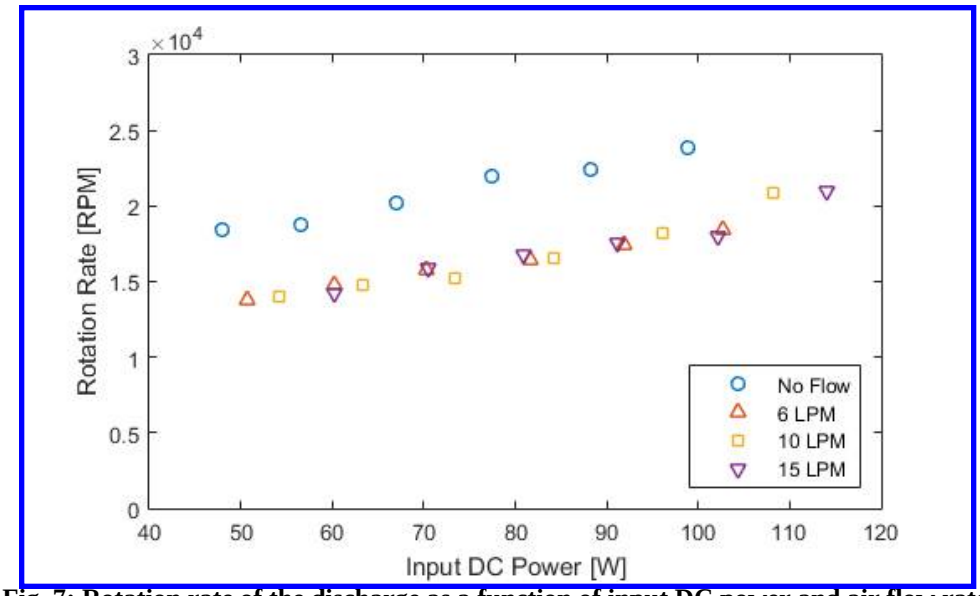

Fig. 7: Rotation rate of the discharge as a function of input DC power and air flow rate.

Table 3: Actuator circuit characteristics.

#	Air Flow Rate [LPM]	DC Current [A]	DC Voltage [V]	DC Power [W]	Discharge Rotation Rate [rpm]
1	0	3.72	18	66.96	20,190
2	6	3.91	18	70.38	15,790
3	10	4.08	18	73.44	15,280
4	15	4.50	18	81.00	16,820

C. Schlieren Images

The heating generated by the plasma filament produced density gradients in the air which were visualized for an air flow rate of 10 LPM through the CAPA swirler using schlieren imaging. The unactuated case was visualized using the residual heat after running the discharge, as the density gradients imposed by the pressurization were insufficient at this flow rate. Sample instantaneous schlieren images of air flow through the swirler without actuation and with actuation at a DC power level of 73W are shown in Fig. 8. Differences in the heating levels make some of the features in the actuated case appear more prominent than those in the unactuated case. However, key differences can be observed between the two cases. For the unactuated case a vortex roll-up of the shear layer is observed, which forms a periodic street of vortex rings. The initially laminar jet is also observed quickly transition to a turbulent flow and small-scale structures become clearly visible a couple of diameters downstream of the orifice. In contrast, the turbulence levels in the actuated case appear significantly larger than those in the unactuated case, especially in the region of flow immediately downstream of the outlet. This flow also exhibits density gradients with a much larger amplitude, which is believed to be produced due to the thermal influences of the plasma emission.

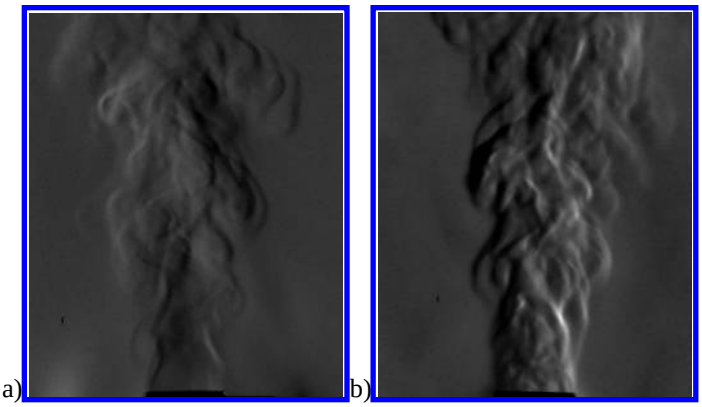

Fig. 8: Instantaneous schlieren images of: a) Air flow of 10 LPM with no actuation; b) Air flow of 10 LPM with actuation.

D. Stereoscopic Particle Image Velocimetry

Time-averaged Stereo-PIV data were acquired across seven evenly-spaced planes centered above the swirler outlet for air flow rates of 10 LPM, 15 LPM, and 20 LPM with and without actuation. For brevity, reconstructions of the flowfield are presented only for air flow rate of 10 LPM. Actuation was provided by a discharge with a counterclockwise rotation direction at a DC power level of 73W. In order to better understand the flow interactions produced by the CAPA swirler, averaged three-component planar velocity data were interpolated using Gaussian process regression to produce a volumetric representation of the air jet velocity field. The swirler central axis was centered at the origin of the *xy*-plane ($x = 0$, $y = 0$), and the exit plane of the air jet was at the $z = -1.7$mm location for all presented plots. Thus, the axial jet velocity was in the positive *z*-direction.

To better understand the salient flow features in the unactuated and actuated air jets, velocity data were extracted across a set of two-dimensional planes, shown in Fig. 9. Four horizontal planes at $z = 0$mm, 10mm, 20mm, and 30mm colored in velocity magnitude contours are presented along with in-plane velocity vectors. In both the actuation and no-actuation cases, the maximum jet velocities are observed immediately outside of the orifice and the associated velocity decreases while the jet lateral extent increases further with axial distance from the outlet. Due to the coaxial configuration of the electrodes, the jet has a double-hump profile, and a local minimum in the jet velocity is observed in the center of the jet, immediately downstream of the wake of the central electrode. For a fixed axial position, the maximum velocity of the jet is observed within the radial region set by the ring-shaped inter-electrode gap.

Several key differences between the unactuated and the actuated cases can be observed in the velocity fields. For the unactuated jet, shown in Fig. 9a, the velocity vectors in the $z = 0$ plane are pointing radially inward toward the center of the jet, indicating that in-plane motion, perpendicular to the main jet velocity, is produced due to air being entrained to the low velocity core of the jet. As the distance from the outlet increases, the velocity deficit in the core of the jet diminishes and the velocity profile becomes more uniform. The in-plane motion, demonstrated by the velocity vectors in the *xy*-plane, also decreases with increasing axial distance from the orifice.

In contrast, for the plasma actuation case in Fig. 9b, the velocity vectors immediately downstream of the jet outlet have a strongly defined clockwise orientation which persists several jet diameters downstream of the jet outlet, such that the trace of this vortical flow behavior can be seen in all presented horizontal planes. Since the shown horizontal sections of the flow are parallel to the discharge rotation plane, the axis of flow rotation coincides with the axis of the discharge rotation. Thus, the plasma rotation is directly linked to the swirling in the air jet. Furthermore, the added tangential velocity component in the swirl-actuated case results in a larger velocity magnitude as compared to the unactuated flow case.

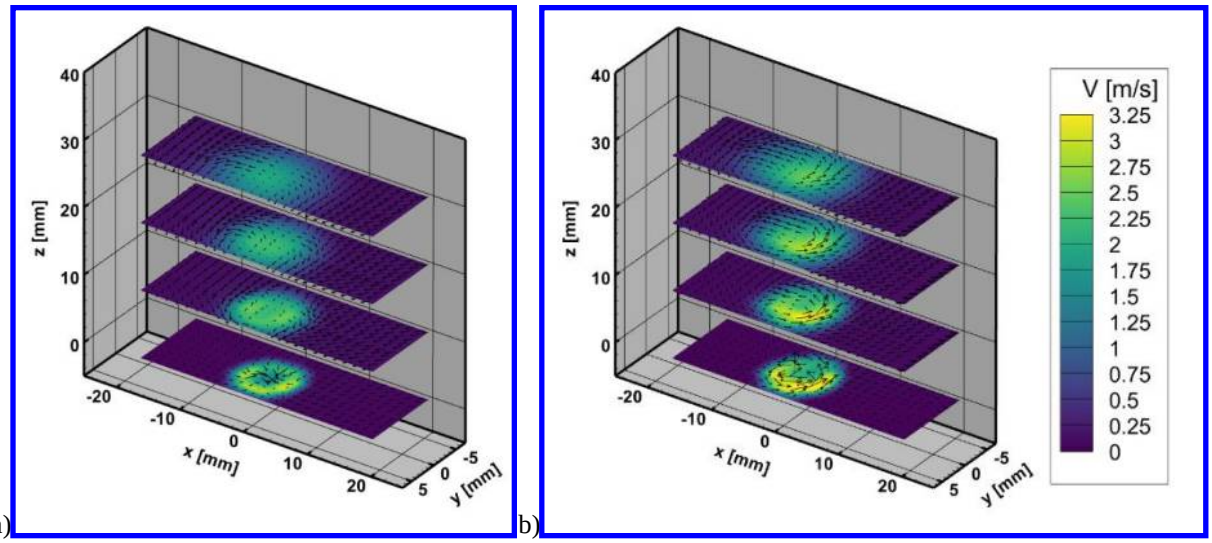

Fig. 9: Horizontal slices of the flow field colored in velocity magnitude and velocity vectors: a) 10 LPM air flow without actuation; b) 10 LPM air flow with actuation.

Horizontal *xy*-planes of vorticity magnitude at z = 0mm, 10mm, 20mm, 30mm, and 40mm are presented, along with a central *xz*-plane, in Fig. 10 for both the actuated and unactuated flows. The vorticity magnitude contours in both cases highlight the shear layers in the flow as the regions of highest vorticity. Due to the coaxial geometry of the CAPA swirler, two concentric shear layers are observed. The first shear layer is located at the outer limit of the air jet where it interacts with the stationary ambient air and induces vortex rollup. This vorticity is concentrated in a thin layer immediately downstream of the jet outlet, and dissipates into a larger region of low vorticity with increased axial distance from the jet outlet. As seen in the velocity fields in Fig. 9, a region of lower flow velocity exists in the wake of the central coaxial electrode. The boundary between this region of lower flow velocity and the high velocity jet forms the inner shear layer observed in the vorticity fields. These main features can be observed in both the actuated and unactuated cases. However, the vorticity in the core of the unactuated jet is noticeably lower than the vorticity in the core of the actuated jet. The core vorticity in the actuated jet also persists farther downstream of the jet outlet. This difference is attributed to the actuation-induced swirling which provides enhanced mixing in the flow and a momentum transport mechanism from the high momentum annular jet region to the low momentum jet core.

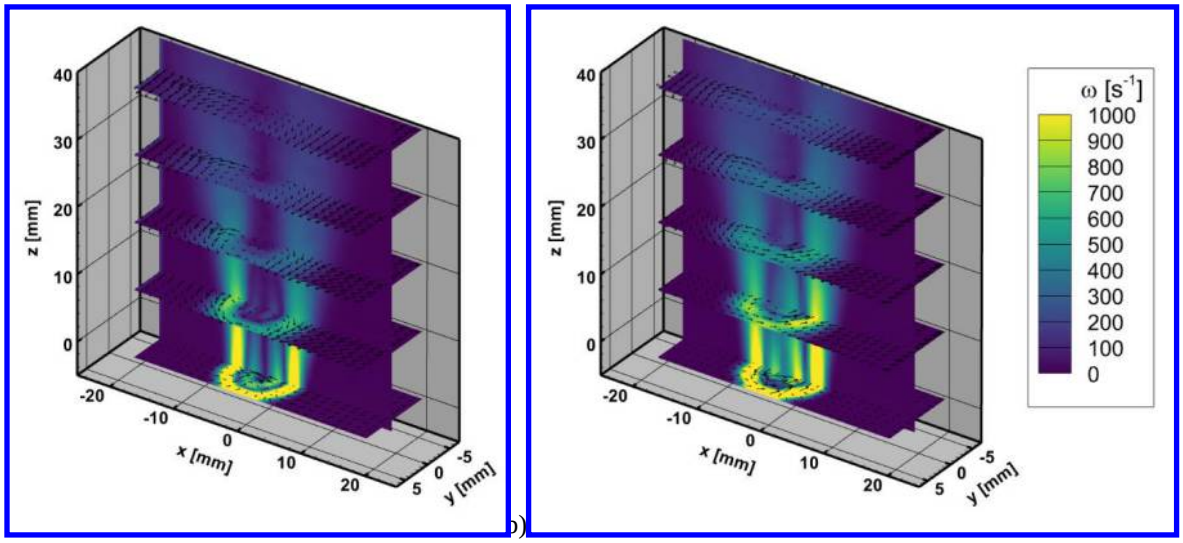

Fig. 10: Planar slices of the flow field colored in vorticity magnitude and velocity vectors: a) 10 LPM air flow without actuation; b) 10 LPM air flow with actuation.

To further characterize the influence of the plasma swirler on the jet flow, the subsequent discussion is concentrated on identifying and quantifying the development of coherent vortex structures in the three-dimensional

flowfield. For this purpose, the current study used the Q-criterion as described by Hunt et al. [53] The Q-criterion is a Galilean-invariant criterion which has historically been used to identify vortices in a three-dimensional incompressible flow. Unlike vorticity magnitude and flow streamlines, it is unaffected by translations of the reference frame. [54,55] The Q-criterion defines a vortex as the excess of rotation relative to strain in the flow. The symmetric strain rate tensor and the antisymmetric rigid body rotation rate tensor are the components of the velocity gradient tensor :

$$\frac{\partial u_i}{\partial x_j} = S_{ij} + \Omega_{ij} = \frac{1}{2}\left(\frac{\partial u_i}{\partial x_j} + \frac{\partial u_j}{\partial x_i}\right) + \frac{1}{2}\left(\frac{\partial u_i}{\partial x_j} - \frac{\partial u_j}{\partial x_i}\right) \quad (5)$$

Therefore, the Q-criterion is defined as:

$$\boldsymbol{Q} = \frac{1}{2}\left(\|\boldsymbol{\Omega_{ij}}\|^2 - \|\boldsymbol{S_{ij}}\|^2\right), \quad (6)$$

which for incompressible flow, equals the second invariant of the velocity gradient tensor. Consequently, vortices are defined as regions where the rotation rate is larger than the strain rate, or Q > 0.

The identified regions of vorticity with a Q-value of Q = 3,500 are shown in Fig. 11 for both the actuated and unactuated cases of 10 LPM air flow through the plasma swirler. These regions were colored in the local value of helicity, which is calculated using the dot product of the velocity and vorticity vectors and quantifies the knottedness of vortex lines in the flow. As such, it can be used as a useful indicator of how the velocity vector field is oriented with respect to the vorticity field. [56] The extreme values of helicity (yellow and purple) correspond to streamwise vorticity and highly three-dimensional flow, and the center values (blue and green) correspond to vorticity normal to the velocity i.e., largely two-dimensional flow.

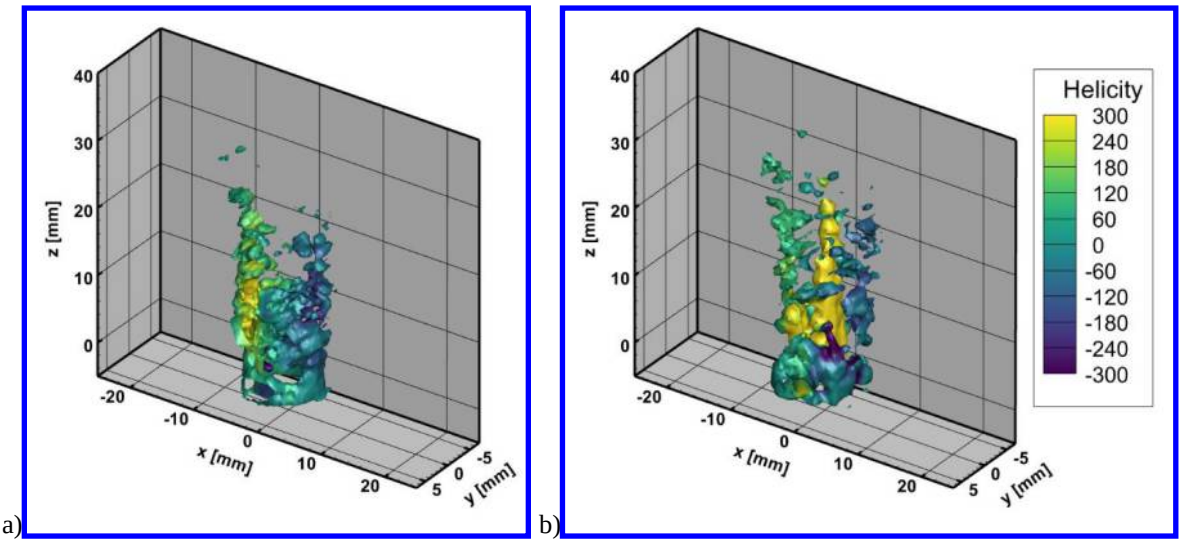

Fig. 11: Isosurfaces of Q = 3,500 colored in relative helicity: a) 10 LPM air flow without actuation; b) 10 LPM air flow with actuation.

As seen from Fig. 11a, a cylindrical region of vorticity along the outer edge of the jet was identified by the Q-criterion for the unactuated air jet case. This region corresponds to the shear layer, a region of concentrated vorticity, between the air jet and the stagnant ambient air previously observed in the vorticity contours of Fig. 10. The large amplitude of shear stress imposed by the velocity profile between the two regions of the flow promotes the formation of vortices which then entrain the surrounding fluid. To further support this observation, the helicity values across this region correspond to velocity and vorticity vectors that are not aligned. The jet flow is in the positive *y*-direction, whereas the vorticity across this interface is associated with to the rolling up of the shear layer, and therefore is in the plane normal to the jet flow. A similar region of vorticity was identified in the actuated air jet case in Fig. 11b, along with a column-shaped region of concentrated vorticity in the core of the jet. This region corresponds to the largest helicity values in the flow. Using the right-hand rule, it can be seen that when the helicity is large and positive, the velocity and vorticity vectors are largely aligned, which corresponds to a counterclockwise flow rotation. The Q-criterion unambiguously shows the central vortex whose existence was initially implied by the flow velocity vectors. This counterclockwise rotation identified in the core of the actuated case is consistent with the counterclockwise discharge rotation. This is a strong indication that the central structure identified by the Q-criterion is the core of a vortex that is a direct consequence of the plasma actuation.

In order to complete the characterization of the plasma swirling on the air jet, turbulence statistics in the form of the Reynolds stress components are discussed in this section for 10 LPM, 15 LPM, and 20 LPM flow rates of air. Since, as seen from Fig. 7, the change of rotation rate with power was relatively low within the range of power levels obtained with the available equipment, the axial jet velocity was varied with flow rate, and the rotation rate of the discharge was approximately kept constant. This allowed different swirl numbers to be achieved across the tested flow rates, however, the variation in the axial velocity also resulted in a variation in the jet Reynolds number. Comparisons of the unactuated and the actuated cases for a given flow rate were made to illustrate the effects on turbulence generation due to the swirl and the added Joule heating at the plasma location. Comparisons across the different tested flow rates reveal the swirl number and Reynolds number effects. Although the flow is ideally axisymmetric, the full data range from -2.5R to 2.5R was presented to acknowledge the existence of non-uniformities in the flow field due to the imperfect central placement of the central electrode in the coaxial configuration. Factors that contributed to the central electrode drift from the center were manufacturing imperfections and thermal expansion. These effects are not significant for the interpretation of the data but are observed in the form of elevated levels of turbulence in the $x/R > 0$ location.

Several boundaries in the jet were identified to delineate specific areas of the flow where the influence of the turbulence fields was linked to the underlying mean field features. Firstly, the jet outer boundary was defined as the location where the gradient of axial velocity increased above zero. In practice, however, an empirically determined small nonzero threshold was used. The outer shear layer location in Fig. 12 was identified using the mean flow '$10\%\Delta V_z$' contour, which is a common metric to define boundaries in free shear layers. [57] The quantity ΔV_z is the difference between primary and secondary stream velocities, which in the particular case is equal to the jet velocity V_z, since the ambient air was stagnant. As there was not a clear interface separating the jet from the central electrode wake, the inner shear layer between these two regions in the flow was defined based on the contour connecting the inflection points between the velocity peaks and the trough in the double hump jet velocity profile at different axial locations. It is argued that the inflection points in the velocity contours represent the regions in the flow that experience highest shear as it identifies the maximum change in the velocity with radial distance. The identified outer jet boundary and shear layer locations are shown in Fig. 12, with solid and dashed black lines respectively, along with the jet axial velocity V_z at the plane of symmetry. Some of the features discussed in Section III.A such as the increase in jet velocity due to the plasma blockage can be observed in Fig. 12. For the unactuated cases, the size of the wake region decreases with increasing flow rate. This reduction, however, is minor as the downstream extent of the wake region decreases from approximately 3.5R to 3R as the jet flow rate is doubled from 10 LPM to 20 LPM. A similar trend is observed in the actuated cases where swirling is present. Additionally, for a fixed flow rate, actuation resulted in a smaller wake region, identified by the inner shear layer boundary, as compared to the unactuated cases. The only exception is the 10 LPM case which is attributed to an overestimation of the downstream extent of the wake region due to a degree of asymmetry in the jet. Comparing the decrease of the wake extent with increasing flow rate in the unactuated case to the decrease of the wake extent due to actuation for a single flow rate, one can see that the decrease in the wake extent for the actuated case cannot be explained solely by a change in the axial jet velocity. Therefore, the decrease in the downstream wake extent is attributed to the main effects of the plasma actuation such as swirl addition and heating.

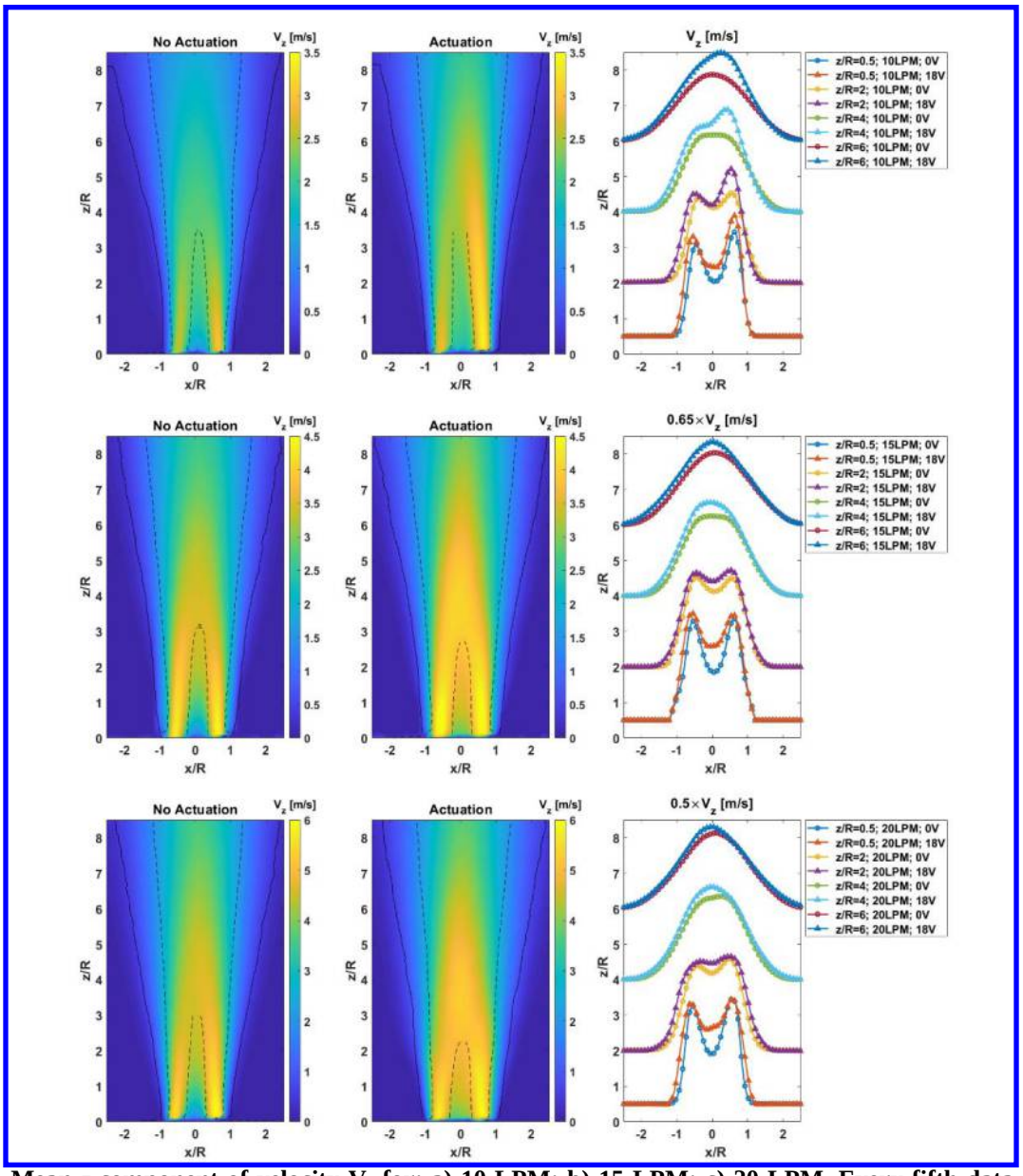

Fig. 12: Mean *z*-component of velocity V_z for: a) 10 LPM; b) 15 LPM; c) 20 LPM. Every fifth data point is shown as marker.

The Reynolds stress tensor R_{ij}, defined as $R_{ij} = \overline{u_i' u_j'}$, has six independent components that represent the product of the fluctuating velocity components. Analytically, due to the axisymmetric configuration of the flow when swirl is not present, the $R_{r\theta}$ and $R_{\theta z}$ components of the Reynolds stress tensor are zero. Experimentally, these components were each measured to be at least an order of magnitude smaller than the other four independent components. In the actuation-on case, when the swirl added a tangential velocity component, disrupting the axial symmetry, the $R_{r\theta}$ and $R_{\theta z}$ components increased in magnitude but remained significantly lower than the other Reynolds stress components. This is explained by the low degree of swirl, seen by the swirl numbers in Table 1. Therefore, these components were not considered a significant contributor to the turbulence fluctuations in the jet and were not used in the discussion for brevity.

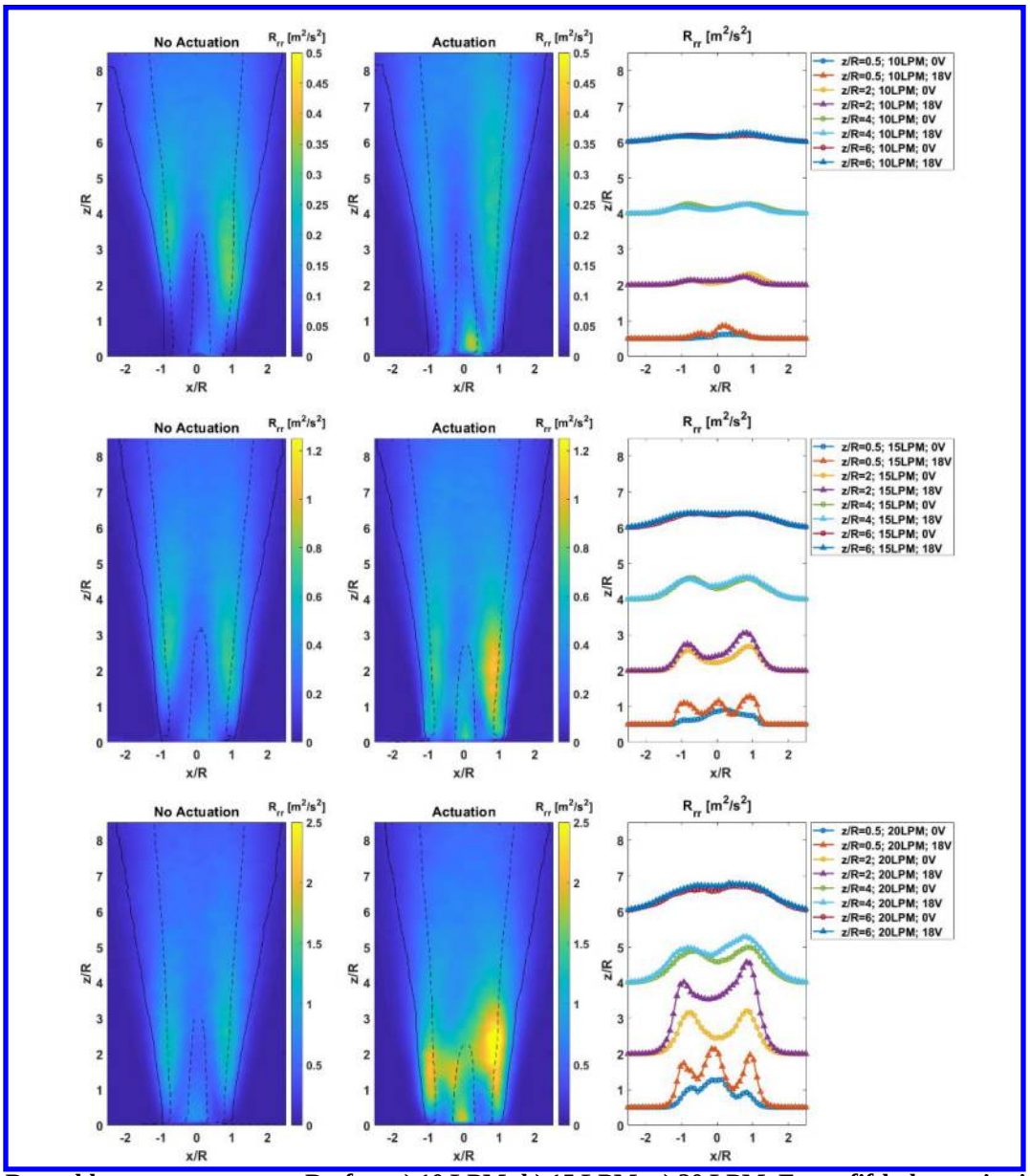

Fig. 13: Reynolds stress component R_{rr} for: a) 10 LPM; b) 15 LPM; c) 20 LPM. Every fifth data point is shown as marker.

The normal Reynolds stress components were presented along with solid black lines depicting the jet outer boundary, and dashed black lines depicting the locations of the inner and outer shear layers. The normal stress components are shown in Fig. 13 through Fig. 15, and the R_{rz} shear component is shown in Fig. 16. The normal stresses for a given air flow rate are all the same order of magnitude which suggests that the turbulence in the shear layer is approximately isotropic. Furthermore, when swirl was introduced, all Reynolds stresses increased in intensity and spatial extent, consistent with previous work on swirl jets. [47,51] As expected, the magnitude of the turbulence intensities is increased with flow rate.

The R_{rr} normal component of the Reynolds stress tensor is shown for the three flow rates in Fig. 13. Immediately at the jet exit, there are three regions of high intensity fluctuations in R_{rr}, seen as peaks in the two-dimensional slices of the data. The central region is located within the wake identified by the inner shear layer contour, whereas the other regions of high intensity fluctuations occur in the outer shear layer. Those outer shear layer fluctuations correspond to the Kelvin-Helmholtz vortex ring shedding as described by Yule. [58] The spatial extent and the magnitude of the fluctuations grow with actuation. The growth in the profile of the Reynolds stress with actuation suggests that the jet grows radially with actuation. Interestingly, the increases in R_{rr} due to actuation are greater as the jet flow rate is

increased. As the distance away from the jet outlet increases, the high intensity fluctuations in the wake region subside. This change in turbulent energy distribution is indicative of a change in the spatial distribution of dominant turbulent structures. At a distance of approximately 3.5-4R away from the jet outlet, the intensities of R_{rr} are at the same levels for both the actuated and unactuated cases and are concentrated in the outer shear layer, indicating the extent of the actuation effect.

In the near field, similar to the R_{rr} component, the $R_{\theta\theta}$ component for the unactuated case has three regions of elevated turbulence coinciding with the outer shear layer boundary and the wake region. When actuation is added, the $R_{\theta\theta}$ intensity is not only amplified, but also two new peaks appear in the space between the wake region and the outer shear layer, which is located immediately above the interelectrode gap. These peaks are seen as a direct effect of the actuation, and the addition of an extra V_θ velocity component. The two outer shear layer peaks are pushed radially outwards with actuation as the jet grows due to the swirl addition. At a distance of 2R downstream of the jet exit, the inner three peaks merge into a plateau region. Farther downstream, at distances greater than 3.5-4R, there is a redistribution of turbulent energy towards the outer shear layer, and the intensities of the Reynolds stresses are at the same levels for both the actuated and unactuated cases.

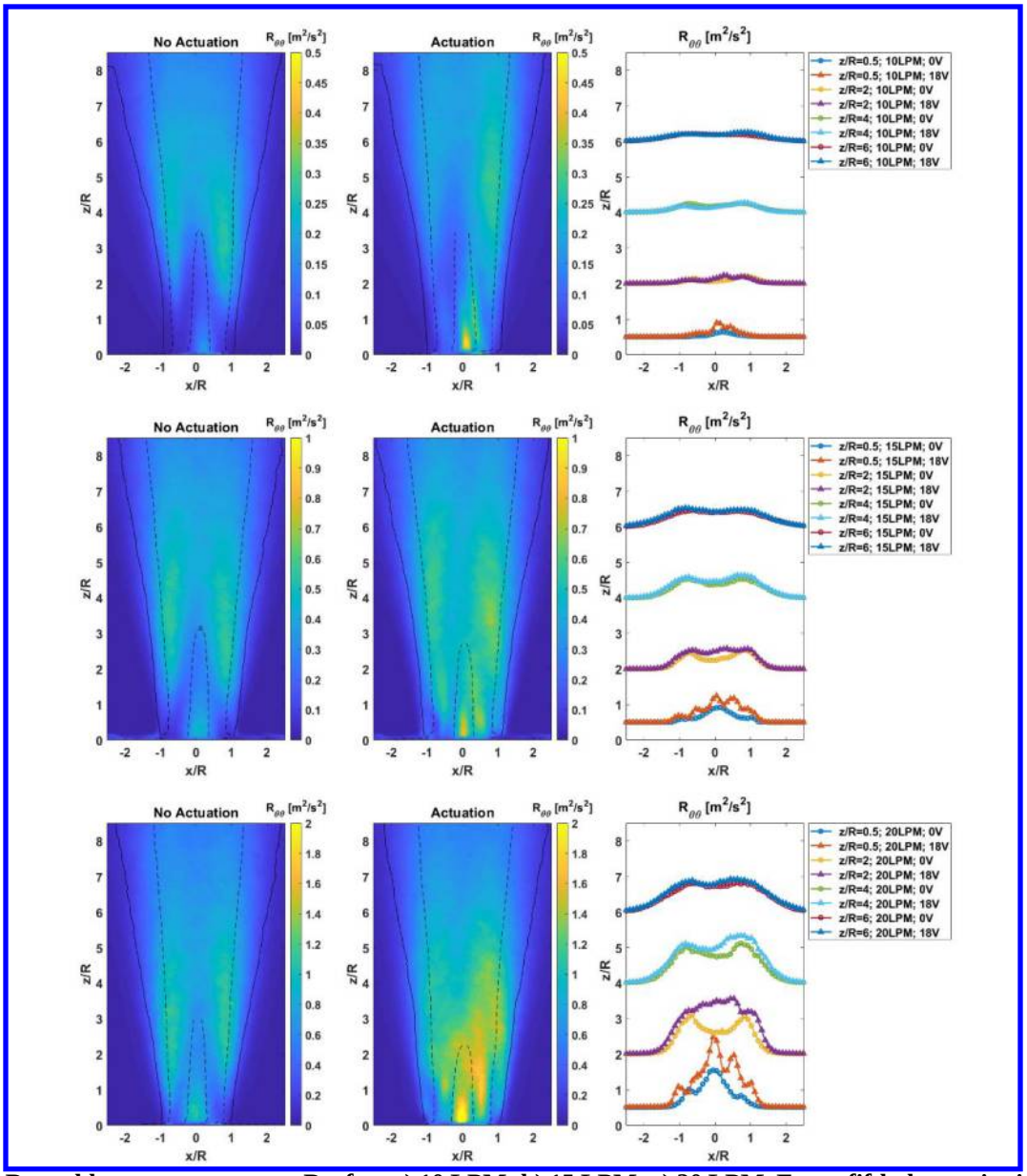

Fig. 14: Reynolds stress component $R_{\theta\theta}$ for: a) 10 LPM; b) 15 LPM; c) 20 LPM. Every fifth data point is shown as marker.

Unlike the other two normal components of the Reynolds stress tensor, the highest fluctuations in R_{zz} (Fig. 15) in the near field occur in the shear layers, and not in the wake region. Similar to the R_{rr} normal stress, the outer peaks correspond to the Kelvin-Helmholtz shedding process due to the interaction of the jet with the ambient air, whereas the inner peaks are located at the interface between the high-speed jet and the low-speed central electrode wake. The fluctuations in the inner shear layer decrease at a distance 2-3R from the jet outlet, as momentum from the jet flow is added to the flow in the wake such that the double hump flow profile takes the form of a top-hat profile and later a Gaussian profile (Fig. 12). Adding actuation to the flow increases the intensity of the inner shear layer and wake turbulence, as well as the lateral extent of the flow. The growth in the R_{rr} peaks with actuation is especially visible in the 20LPM air flow case. These effects are observed to persist up to 2.5R away from the jet outlet.

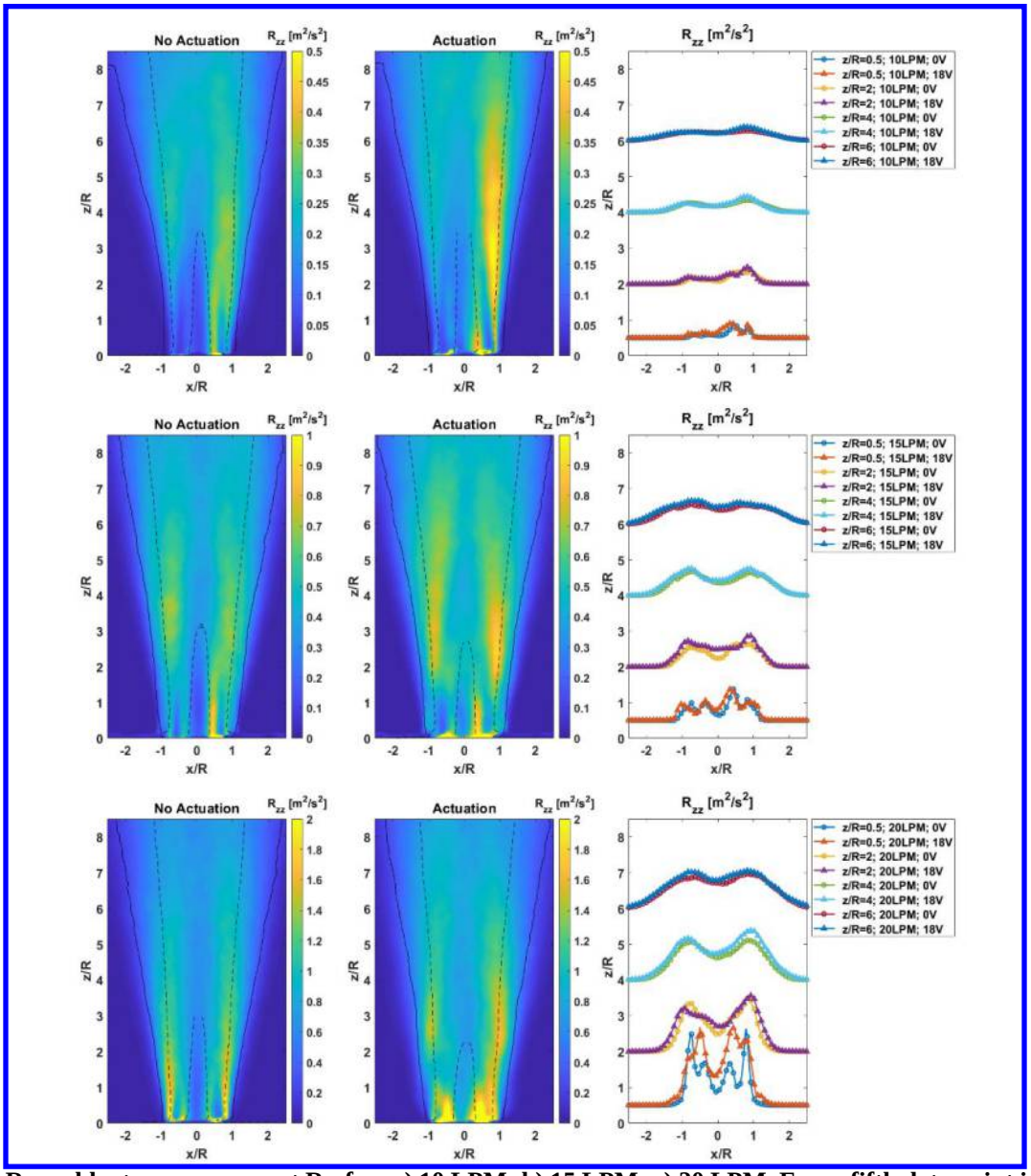

Fig. 15: Reynolds stress component R_{zz} for: a) 10 LPM; b) 15 LPM; c) 20 LPM. Every fifth data point is shown as marker.

The major contribution to the shear stress R_{rz}, as argued by Yule, [58] is due to the fluid movement induced by large eddy structures. Yule correlated these large eddies to peaks in the temporal signals of the V_z and V_r velocity components. The R_{rz} shear components of the Reynolds stress tensor in the current study exhibit similar behavior with and without actuation. The addition of actuation increases the turbulence intensity magnitudes across all flow rates.

Positive intensity is observed in the outer shear layer, whereas negative intensity is observed in the inner shear layer. The increase in spatial extent with actuation observed in the other stress components is also seen in the near field of R_{rz}.

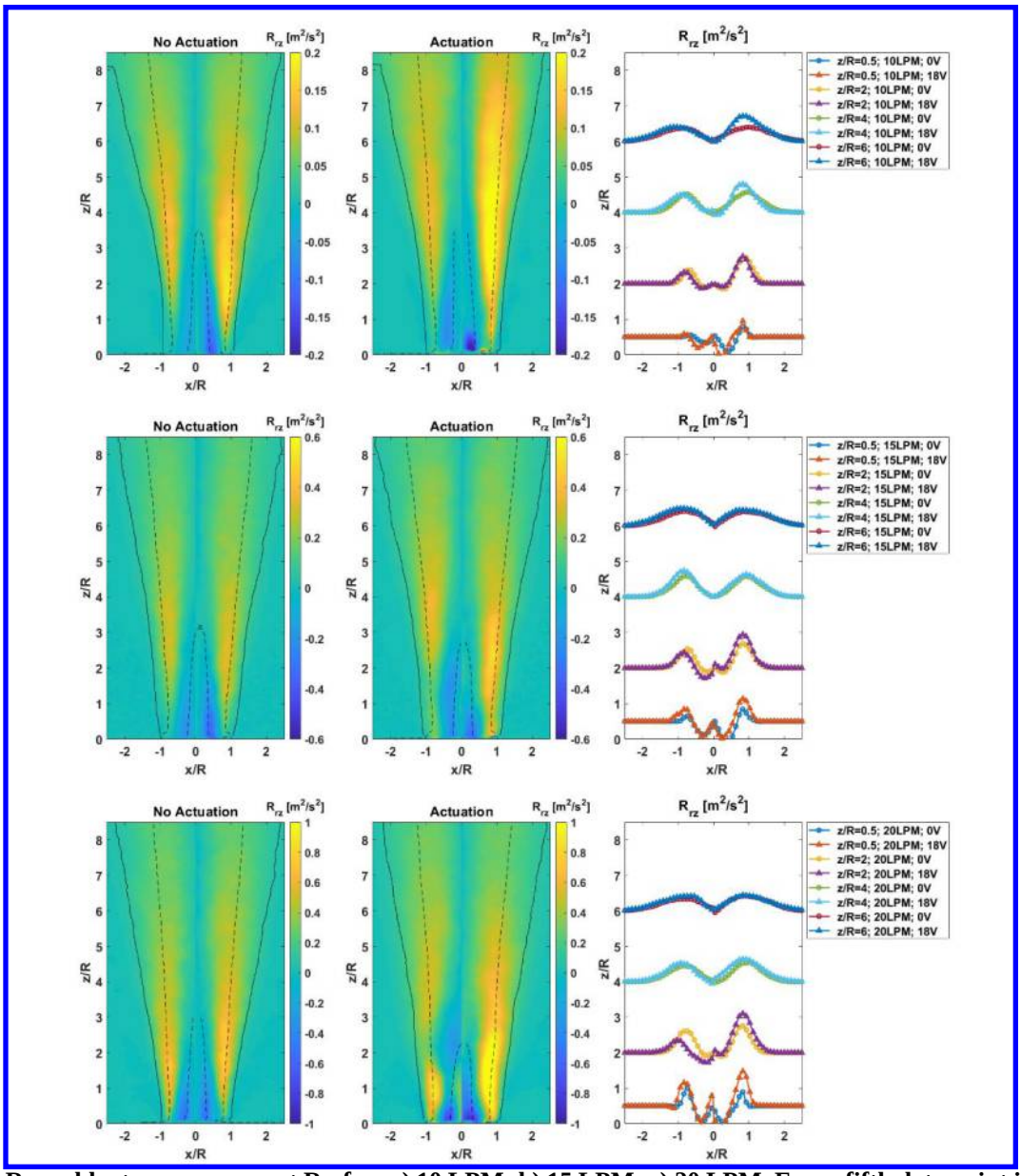

Fig. 16: Reynolds stress component R_{rz} for: a) 10 LPM; b) 15 LPM; c) 20 LPM. Every fifth data point is shown as marker.

IV. Conclusions

The swirl production in an axisymmetric jet of air, having a magnetically-driven nonequilibrium gliding arc plasma discharge, was studied. Jet parameters such as Reynolds number and swirl number were characterized along with plasma blockage effects. It was established that the plasma actuation included effects comparable to a low-swirl jet.

A qualitative description of the thermal effects and the turbulence levels in the actuated and unactuated jets was provided using Schlieren visualization. Stereo-PIV was used to quantitatively study the jet and compare the velocity fields of the unactuated and the actuated cases. Horizontal sections of the velocity fields were used to show the velocity

distribution in the plane parallel to the jet outlet, and therefore show the swirling of the velocity vectors of the mean flow when actuation was present. A detailed description of the vorticity region was made by showing vorticity magnitude and Q-criterion contours. These data showed that the averaged flow for the actuated case was swirled in the direction of discharge rotation, whereas swirl was absent from the unactuated flow case. Two major coherent structures were identified in the averaged stereo-PIV velocity data using the Q-criterion. A region of vorticity was identified at the shear layer location for both the actuated and the unactuated case. A column-like structure, which was absent from the unactuated case, was identified by the Q-criterion in the actuated case at the location of the center of the swirling flow.

The turbulence statistics of the jets revealed regions of high intensity fluctuations concentrated in the shear layers. These local regions of turbulent fluctuations were related to the Kelvin-Helmholtz shedding process due to the interaction of the jet with lower momentum air regions. These peak magnitudes were amplified with actuation for all considered flow rates. The plasma actuation added regions of elevated turbulence immediately above the interelectrode gap to the normal components of the Reynolds stress in the tangential direction. This, along with the radial expansion of the jet, was associated with the swirling due to the plasma actuation.

V. Acknowledgements

This work was supported by a DOE SBIR Contract DE-SC0020814 that is monitored by Dr. Nirmol Podder. The authors, the University of Illinois, and CU Aerospace would like to thank DOE for their support of this project.

References

[1] Gupta, A. K., Lilley, D. G., Syred, N., "Swirl flows," Abacuss Press, London, 1984.
[2] Lilley, D. G., "Swirl Flows in Combustion: A Review," AIAA Journal, Vol. 15, No. 8, pp. 1063-1078, Aug 1977.
[3] Lieuwen, T., Torres, H., Johnson, C., Zinn, B.T., "A Mechanism of Combustion Instability in Lean Premixed Gas Turbine Combustors," J. Eng. Gas Turbines Power, Vol. 123, 182-189, Jan 2001.
https://doi.org/10.1115/1.1339002
[4] Oberleithner, K., Paschereit, C.O., Seele, R., Wygnanski, I., "Formation of Turbulent Vortex Breakdown: Intermittency, Criticality, and Global Instability," AIAA Journal, Vol. 50, No. 7, pp. 1437-1452, Jul 2012.
DOI: 10.2514/1.J050642
[5] Jalalatian, N., Tabejamaat, S., Kashir, B., and EidiAttarZadeh, M., "An Experimental Study on the Effect of Swirl Number on Pollutant Formation in Propane Bluff-body Stabilized Swirl Diffusion Flames," Physics of Fluids Vol.31, 059901, Apr 2019.
https://doi.org/10.1063/1.5089683
[6] Syred, N., Beer, J. M., "Combustion in Swirling Flows: A Review," Combustion and Flame, Vol. 23, Issue 2, pp. 143‑201, 1974.
https://doi.org/10.1016/0010-2180(74)90057-1
[7] Oberleithner, K., Sieber, M., Nayeri, C.N., Paschereit, C.O., Petz, C., Hege, H.-C., Noack, B.R., Wygnanski, I., "Three-dimensional Coherent Structures in a Swirling Jet Undergoing Vortex Breakdown: Stability Analysis and Empirical Mode Construction," Journal of Fluid Mechanics, Vol. 679, pp. 383-414, 2011.
doi:10.1017/jfm.2011.141
[8] Canepa, E., Cattanei, A., Lengani, D., Ubaldi, M., Zunino, P., "Experimental Investigation of the Vortex Breakdown in a Lean Premixing Prevaporizing Burner," Journal of Fluid Mechanics, Vol. 768, Cambridge University Press, Apr 2015.
https://doi.org/10.1017/jfm.2015.55
[9] Billant, P., Chomaz, J.-M., Huerre, P., "Experimental Study of Vortex Breakdown in Swirling Jets," Journal of Fluid Mechanics, Vol. 376, pp. 183-219, Cambridge University Press, 1998.
DOI: https://doi.org/10.1017/jfm.2015.55
[10] Sarpkaya, T., "On Stationary and Travelling Vortex Breakdowns," Journal of Fluid Mechanics, Vol. 45, Issue 3, pp. 545-559, Cambridge University Press, Feb 1971.
DOI: https://doi.org/10.1017/S0022112071000181

[11] Lucca-Negro, O., O'Doherty, T., "Vortex Breakdown: A Review," Progress in Energy and Combustion Science, Vol. 27, Issue 4, pp. 431–481, 2001.
https://doi.org/10.1016/S0360-1285(00)00022-8
[12] Tangirala, V., Driscoll, J. F., "Temperatures Within Non-premixed Flames: Effects of Rapid Mixing due to Swirl," Combustion Science and Technology, Vol. 60, pp. 143-162, Mar 1988.
DOI: 10.1080/00102208808923981
[13] Syred, N., "A Review of Oscillation Mechanisms and the Role of the Precessing Vortex Core (PVC) in Swirl Combustion Systems," Progress in Energy and Combustion Science, Vol. 32, Issue 2, pp. 93-161, 2006.
https://doi.org/10.1016/j.pecs.2005.10.002
[14] Froud, D. Y., Fick, W., Bowen, P. J., O'Doherty, T., Syred, N., "Characterization of Industrial Swirl Burners for Efficient Combustion of Low Calorific Value Gases," Proceedings of The Institute of Energy Conference, London, UK, Dec 4-5, 1995.
[15] Froud, D., O'Doherty, T., Syred, N., "Phase averaging of the precessing vortex core in a swirl burner under piloted and premixed combustion conditions," Combustion and Flame, Vol. 100, Issue 3, pp. 407-410, February 1995.
https://doi.org/10.1016/0010-2180(94)00167-Q
[16] Gorbunova, A., Klimov, A., Molevich, N., Moralev, I., Porfirieva, D., Sugak, S., Zavershinskii, I., "Precessing Vortex Core in a Swirling Wake with Heat Release," International Journal of Heat and Fluid Flow, Vol. 59, pp. 100-108, Jun 2016.
https://doi.org/10.1016/j.ijheatfluidflow.2016.03.002
[17] Syred, N., Fick, W., O'Doherty, T., Griffiths, A. J., "The Effect of the Precessing Vortex Core on Combustion in a Swirl Burner," Combustion Science and Technology, Vol. 125, pp. 139-157, Mar 1997.
https://doi.org/10.1080/00102209708935657
[18] Farokhi, S., Taghavi, R., Rice, E. J., "Effect of Initial Swirl Distribution on the Evolution of a Turbulent Jet," AIAA Journal, Vol. 27, No. 6, pp. 700-706, 1989.
https://doi.org/10.2514/3.10168
[19] Gilchrist, R. T., Naughton, J. W., "Experimental Study of Incompressible Jets with Different Initial Swirl Distributions: Mean Results," AIAA Journal, Vol. 43, No. 4, pp. 741-751, Apr 2005.
https://doi.org/10.2514/1.3295
[20] Tang, J., Zhao, W., and Duan, Y., "In-Depth Study on Propane-Air Combustion Enhancement with Dielectric Barrier Discharge," IEEE Transactions on Plasma Science, Vol. 38, No. 12, Dec 2010.
DOI: 10.1109/TPS.2010.2084597
[21] Di Sabatino, F., and Lacoste, D. A., "Enhancement of the Lean Stability and Blow-off Limits of Methane-air Swirl Flames at Elevated Pressures by Nanosecond Repetitively Pulsed Discharges," Journal of Physics D: Applied Physics, Vol. 53, No. 35, Aug 2020.
DOI: 10.1088/1361-6463/ab8f54
[22] Vincent-Randonnier, A., Larigaldie, S., Magre, P., and Sabel'nikov, V., "Plasma Assisted Combustion: Effect of a Coaxial DBD on a Methane Diffusion Flame," Plasma Sources Science and Technology, Vol. 16, No. 1, Dec 2006.
https://doi.org/10.1088/0963-0252/16/1/020
[23] Lacoste, D. A., and Moeck, J. P., "Effect of Nanosecond Glow Discharges on a Lean Premixed V-Flame," IEEE Transactions on Plasma Science, Vol. 42, No. 12, Oct 2014.
[24] Bozhenkov, S. M., Starikovskaia, S. M., and Starikovskii, A. Y., "Nanosecond Gas Discharge Ignition of H2- and CH4 Containing Mixtures," Combustion and Flame, Vol. 133, No. 1-2, pp. 133-146, Apr 2003.
[25] Starikovskaia, S. M., Kukaev, E. N., Kuksin, A. Y., Nudnova, M. M., and Starikovskii, A. Y., "Analysis of the Spatial Uniformity of the Combustion of Gaseous Mixture Initiated by Nanosecond Discharge," Combustion and Flame, Vol. 139, No. 3, Nov. 2004, pp. 177-187.
doi:10.1016/j.combustflame.2004.07.005
[26] Takita, K., "Ignition and Flame-Holding by Oxygen, Nitrogen and Argon Plasma Torches in Supersonic Airflow," Combustion and Flame, Vol. 128, No. 3, pp. 301-313, Feb 2002.
doi:10.1016/S0010-2180(01)00354-6
[27] Takita, K., Moriwaki, A., Kitagawa, T., and Masuya, G., "Ignition of H2 and CH4 in High Temperature Airflow by Plasma Torch," Combustion and Flame, Vol. 132, No. 4, pp. 679-689, Mar 2003.
doi:10.1016/S0010-2180(02)00518-7
[28] Zaidi, S. H., Smith, T., Macheret, S., and Miles, R. B., "Snowplow Surface Discharge in Magnetic Field for High Speed Boundary Layer Control," 44th AIAA Aerospace Sciences Meeting and Exhibit 9 - 12 January 2006, Reno, Nevada, AIAA Paper 2006-1006, 2006.
https://doi.org/10.2514/6.2006-1006

[29] Braun, E. M., Lu, F. K., and Wilson, D. R., "A Critical Review of Electric and Electromagnetic Flow Control Research Applied to Aerodynamics," 39th Plasmadynamics and Lasers Conference, 23 - 26 June 2008, Seattle, Washington, AIAA Paper 2008-3788, 2008.
https://doi.org/10.2514/6.2008-3788
[30] Nishihara, M., Jiang, N., Rich, J. W., Lempert, W. R., Adamovich, I. V., Gogineni, S., "Low-Temperature Supersonic Boundary Layer Control Using Repetitively Pulsed MHD Forcing," Physics of Fluids, vol. 17, 2005, pp. 106102-106102-12.
https://doi.org/10.1063/1.2084227
[31] Bityurin, V., Bocharov A., Klement'eva, I., and Klimov, A., "Experimental and Numerical Study of MHD Assisted Mixing and Combustion," 44th AIAA Aerospace Sciences Meeting and Exhibit, 9 - 12 January 2006, Reno, Nevada, AIAA Paper 2006-1009, 2006.
https://doi.org/10.2514/6.2006-1009
[32] Balcon, N., Benard, N., Braud, P., Mizuno, A., Touchard, G., and Moreau, E., "Prospects of Airflow Control by a Gliding Arc in a Static Magnetic Field." Journal of Physics D: Applied Physics, Vol. 41, No. 20, September 2008.
doi:10.1088/0022-3727/41/20/205204
[33] Choi, Y.-J., Gray. M., Sirohi. J., and Raja, L. L., "Static Stall Alleviation Using a Rail Plasma Actuator." Journal of Physics D: Applied Physics, Vol. 51, No. 26, June 2018.
https://doi.org/10.1088/1361-6463/aac7b2
[34] Choi, Y.-J., Gray. M., Sirohi. J., and Raja, L. L., "Measurement of Velocity Induced by a Propagating Arc Magnetohydrodynamic Plasma Actuator." 55th AIAA Aerospace Sciences Meeting, 9 - 13 January 2017, Grapevine, Texas.
https://doi.org/10.2514/6.2017-0156
[35] Pafford, B., Sirohi, J., and Raja, L. L., "Propagating-Arc Magnetohydrodynamic Plasma Actuator for Directional High-Authority Flow Control in Atmospheric Air," J. Phys. D: Appl. Phys., Vol. 46, No. 48, 2013, pp. 485208.
https://doi.org/10.1088/0022-3727/46/48/485208
[36] Hristov, G. K., Ansell, P. J., Zimmerman, J. W., Carroll, D. L., "Experimental Characterization of a Novel Cyclotronic Plasma Actuator," AIAA Journal, Vol. 58, No. 2, Feb 2020.
https://doi.org/10.2514/1.J058708
[37] Kalra, C., Gutsol, A., and Fridman, A., "Gliding Arc Discharges as a Source of Intermediate Plasma for Methane Partial Oxidation," IEEE Transactions on Plasma Science, Vol. 33, No. 1, pp. 32–41, Feb 2005.
doi:10.1109/TPS.2004.842321
[38] Ombrello, T., Ju, Y., Gangoli, S., Gutsol, A., and Fridman, A., "Ignition Enhancement Using Magnetic Gliding Arc," 45th AIAA Aerospace Sciences Meeting and Exhibit, 8 - 11 January 2007, Reno, Nevada.
[39] Ombrello, T., Qin, X., and Ju, Y., Gutsol, A., Fridman, A., and Carter, C., "Combustion Enhancement via Stabilized Piecewise Nonequilibrium Gliding Arc Plasma Discharge," AIAA Journal, Vol. 44, No. 1, January 2006.
DOI: 10.2514/1.17018
[40] Fridman, A., Gutsol, A., Gangoli, S., Ju, Y., and Ombrello, T., "Characteristics of Gliding Arc and Its Application in Combustion Enhancement," Journal of Propulsion and Power, Vol. 24, No. 6, November–December 2008.
DOI: 10.2514/1.24795
[41] Zimmerman, J. W., and Carroll, D. L., "Plasma Assisted Combustion Actuators with Arc Breakdown in a Magnetic Field," AIAA Aviation 2019 Forum, 17-21 June 2019, Dallas, Texas.
[42] Zimmerman, J. W., Carroll, D. L., Hristov, G., Vahora, M., and Ansell, P. J., "Circuit Studies for Cyclotronic Plasma Actuators," AIAA Aviation 2019 Forum, Dallas, Texas, Jun 2019.
https://doi.org/10.2514/6.2019-2997
[43] Zimmerman, J., Hristov, G., Carroll, D., Ansell, P. "Development of a Plasma Actuator with Arc Breakdown in a Magnetic Field," 2018 AIAA Aerospace Sciences Meeting, 8-12 January 2018, Kissimmee, Florida, AIAA Paper 2018-1555, 2018.
https://doi.org/10.2514/6.2018-1555
[44] Raffel, M., Willert, C., Kompenhans, J., "Particle Image Velocimetry: A Practical Guide," Springer-Verlag, Berlin, 1998, pp. 174–184.
[45] Hinsch, K. D., "Three-dimensional Particle Velocimetry," Meas. Sei. Tech., 6, pp. 742-753, 1995.
[46] Prasad, A. K., Jensen, K., "Scheimpflug Stereocamera for Particle Image Velocimetry to Liquid Flows," Appl. Optics, 34, pp. 7092-7099, 1995.
[47] Toh, I. K., Honnery, D., Soria, J., "Axial Plus Tangential Entry Swirling Jet," Experiments in Fluids, Vol. 48, pp. 309-325, 2010.

DOI 10.1007/s00348-009-0734-2
[48] Panda, J., McLaughlin, D. K., "Experiments on the Instabilities of a Swirling Jet," Physics of Fluids, Vol. 6, Issue 1, pp. 263-276, 1994.
https://doi.org/10.1063/1.868074
[49] Billant, P., Chomaz, J.-M., Huerre, P., "Experimental Study of Vortex Breakdown in Swirling Jets," Journal of Fluid Mechanics, Vol. 376, pp. 183–219, Cambridge University Press, 1998.
DOI: https://doi.org/10.1017/jfm.2015.55
[50] Gallaire, F., Chomaz, J.M., "Mode Selection in Swirling Jet Experiments: a Linear Stability Analysis," Journal of Fluid Mechanics, Vol. 494, pp. 223–253, Cambridge University Press, 2003.
DOI: 10.1017/S0022112003006104
[51] Liang, H., Maxworthy, T., "An Experiment Investigation of Swirling Jets," Journal of Fluid Mechanics, Vol. 525, pp. 115-159, Cambridge University Press, 2005.
DOI: 10.1017/S0022112004002629
[52] Adams, V. W., "The Influence of Gas Streams and Magnetic Fields on Electric Discharges. PART 2: The Shape of an Arc Rotating Round an Annular Gap," Ministry of Aviation, Aeronautical Research Council Current Papers, C.P. No. 743, London, Sep 1963.
[53] Hunt, J., Wray, A., and Moin, P., "Eddies, Streams, and Convergence Zones in Turbulent Flows," Center for Turbulence Research, Proceedings of the Summer Program, Stanford Univ., Stanford, CA, 1988, pp. 193-202.
[54] Rockwood, M. P., Taira, K., & Green, M. A., "Detecting Vortex Formation and Shedding in Cylinder Wakes Using Lagrangian Coherent Structures", 2017 AIAA Journal, 55(1), 15-23.
https://doi.org/10.2514/1.J055051
[55] Chakraborty, P., Balachandar, S., and Adrian, R, "On the Relationships Between Local Vortex Identification Schemes" 2005, Journal of Fluid Mechanics, 535, 189-214.
https://doi:10.1017/S0022112005004726
[56] Levy, Y., Degani, D., and Seginer, A., "Graphical Visualization of Vortical Flows by Means of Helicity," AIAA Journal, Vol. 28, No. 8, August 1990.
https://doi.org/10.2514/3.25224
[57] Kim, K. U., Elliott, G. S., and Dutton, J. C., "Three-Dimensional Experimental Study of Compressibility Effects on Turbulent Free Shear Layers," AIAA Journal, Vol. 58, No. 1, 2020, pp. 133–147.
DOI:10.2514/1.J058556
[58] Yule, A.J., "Large-scale Structure in the Mixing Layer of a Round Jet," Journal of Fluid Mechanics, Vol. 89, Issue 3, pp. 413-432, Cambridge University Press, Dec 1978.
DOI: https://doi.org/10.1017/S0022112078002670